Available online at www.sciencedirect.com

ScienceDirect

Ceramics International 40 (2014) 3611–3618

CERAMICS INTERNATIONAL

www.elsevier.com/locate/ceramint

Thermal shock behaviour of α:β-SiAlON–TiN composites

Nurcan Calis Acikbas[a,*], Sermet Tegmen[a], Selcuk Ozcan[b], Gokhan Acikbas[c]

[a]Department of Mechanical and Manufacturing Engineering, Bilecik S.E. University, Bilecik, Turkey
[b]Department of Chemical and Process Engineering, Bilecik S.E. University, Bilecik, Turkey
[c]Vocational School, Metallurgy Program, Bilecik S.E. University, Turkey

Received 18 August 2013; received in revised form 13 September 2013; accepted 14 September 2013
Available online 20 September 2013

Abstract

α:β-SiAlON and 10, 17, and 25 wt% TiN particle reinforced composites were produced by a gas pressure sintering method. The densification behavior, phase and microstructural evolution, mechanical and thermal shock behavior of materials were investigated. The TiN incorporation had significant influence on the matrix microstructure and improved fracture toughness of the material. The highest fracture toughness was obtained for the composite with 25 wt% TiN (K_{1c}: 8.2 ± 0.2 MPa $m^{1/2}$). SiAlON–TiN composites showed lower crack formation and propagation compared to the monolithic SiAlON. Above 700 °C passive oxidation took place and provided crack healing by filling the cracks with TiO_2, and the thermal shock resistance behavior was improved.

Keywords: SiAlON–TiN composites; Thermal shock; Fracture toughness; Oxidation

1. Introduction

Silicon nitride based ceramics (Si_3N_4 and SiAlON) have been regarded as one of the promising engineering ceramic materials due to their high strength, hardness, corrosion and wear resistance, and superior temperature properties [1–4]. However, commercial silicon nitride ceramics still posses several inadequacies such as insufficient resistance to brittle fracture, and inferior thermal shock resistance. An essential improvement in the mechanical properties and thermal shock resistance of the silicon nitride ceramics can be brought about by the incorporation of a second phase into ceramic matrix [5,6]. The addition of secondary phases can also improve the resistance to crack initiation and propagation, rendering the silicon nitride ceramics highly utilizable [7–9].

It is known that TiN particles dispersed within the Si_3N_4 matrix improve the fracture toughness of silicon nitride [10–17]. In addition, TiN incorporation improves the chemical resistance and electrical conductivity [18–22]. Considering the potential applications of SiAlON based materials, studies on the effect of thermal cycling on the mechanical and thermal properties are of paramount importance. However, in the literature very few studies have been reported, especially on the thermal shock properties of TiN reinforced silicon nitride based ceramics [23]. As an example of a practical application, SiAlON–TiN cutting tools are being employed extensively in metal machining where the ceramic components are subjected to rapid temperature changes for which the thermal shock resistance is one the most important parameters of durability. Therefore, it proves necessary to reveal the effects of the amount of TiN incorporation in the ceramic matrix on the thermal shock behavior.

Resistance to mechanical weakening or fracture under enduring and repetitive sudden surface temperature changes is termed thermal shock resistance. The thermal shock resistance of brittle materials is governed by two groups of parameters which are $\sigma_f/E\alpha$ and k, where σ_f is the fracture strength, E is the elastic modulus, α is the coefficient of linear expansion, and k is the thermal conductivity. Thermal shock resistance increases with increasing $\sigma_f/E\alpha$ and k. Weibull's statistical theory introduced the maximum risk of the rupture criterion for failure based on the fact that the flaws that exist in any material prevent it from reaching the potential strength in a strength test. Dispersion of flaws in

*Corresponding author. Tel.: +90 228 214 1428; fax: +90 228 214 1427.
E-mail address: nurcan.acikbas@bilecik.edu.tr (N.C. Acikbas).

0272-8842/$ - see front matter © 2013 Elsevier Ltd and Techna Group S.r.l. All rights reserved.
http://dx.doi.org/10.1016/j.ceramint.2013.09.064

length and density causes the often observed dispersion of test results. The theory relates the stress in each infinitesimal element to its contribution to risk of rupture, and the stresses tend to amplify near the flaw tips increasing the risk of rupture [24].

In the worst-case model studied by Hasselman, that is, when the whole body is under maximum stress, the critical temperature difference required for crack propagation goes through a minimum with increasing crack length. There is a region of crack instability bound by lower and upper initial crack lengths, and it encompasses a wider range of initial crack lengths as the temperature difference increases. After crack initiation has started the rate of strain energy release exceeds the surface fracture energy, and the excess energy appears as the kinetic energy of the propagating crack. At a critical temperature difference kinetic crack propagation starts, and the crack length rapidly reaches its upper limit of instability with a corresponding abrupt decrease in material strength. However, the crack propagation halts having reached its subcritical value. Only after temperature difference or thermal stresses reach a second critical value, the crack restarts to propagate in a quasi-static manner, therefore, material strength gradually decreases by increasing thermal stresses. Between the two critical temperature differences the crack length and hence the material strength do not change [25].

Various methods have been developed to assess the thermal shock behavior of such ceramics. Most of them are based on the determination of the loss of strength in a flexural test after a number of heating–cooling cycles [26,27]. Obviously, these methods are both time-consuming and costly. Andersson and Rowcliffe [28] developed an indentation-quench method to determine the thermal shock properties of ceramics. This method provides an efficient way to determine and compare the thermal shock resistance of different materials by measuring the growth of cracks on the sample in a Vickers hardness test [29]. Pettersson et al. applied this method to measure the thermal shock resistances properties of α/β-SiAlONs [30] and β-SiAlONs [31].

In this manuscript, densification during sintering, microstructural and phase evolution, hardness, toughness and thermal shock resistance of SiAlON–TiN composites were investigated for varying amounts of TiN incorporation (10, 17 and 25 wt%).

2. Materials and methods

2.1. Preparation of materials

SiAlON and SiAlON–TiN composites which contain different amounts of TiN (10, 17 and 25 wt%) were prepared to evaluate the thermal shock properties. $25\alpha^{1}$:$75\beta^{1}$-SiAlON compositions were designed by using multi-cation system (9Er:0.5Sm:0.5Ca). The total amount of additives was kept constant at 2.5 mol%. The composition of SiAlON in the sample with nominally $n=1.3$ and $m=1.25$ has a lower x value, as would be expected ($x=m/3=0.416$) and z value is 0.7.

Commercially available powders that were used as starting materials to produce SiAlON and SiAlON–TiN are as follows: high purity α-Si_3N_4 powder (E-10 grade, UBE Co. Ltd., Japan) with 1.4 wt% O content, high purity AlN powder (H Type, Tokuyama Corp. Japan) containing 1.6 wt% O, Al_2O_3 (Alcoa A16-SG, Pittsburgh, USA), Er_2O_3 (>99.99%, Treibacher, Austria), Sm_2O_3 (>99.9%, Stanford Materials Corp., USA), $CaCO_3$ (>99.75%, Reidel-de Haen, Germany) and TiN powder with average particle size of 1–2 μm (>99% pure, H.C. Starck, Grade C, Berlin, Germany).

The slurries with the compositions given above were prepared by wet milling in isopropyl alcohol using Si_3N_4 balls. The slurries were then dried using a rotary evaporator and sieved with a mesh size of 250 μm. The powders were uniaxially pressed to a maximum pressure of 25 MPa, and subsequently cold isostatically pressed at 300 MPa to increase the green density. The pellets were sintered using a two-step gas pressure sintering cycle with a maximum of 2.2 MPa nitrogen gas pressure at 1890 °C for 90 min and then the furnace was allowed to cool at a rate of 5 °C/min.

2.2. Characterization techniques

The densities of the sintered specimens were measured according to Archimedes' principle. Before the mechanical and microstructural studies, the specimens were polished by standard diamond polishing techniques down to 1 μm diamond suspension. The hardness ($HV10$) and indentation fracture toughness (K_{1C}) at room temperature were obtained with a Vickers diamond indenter, using a 98 N load. The Vickers hardness (HV) was calculated by the following equation (Evans and Charles) [32]:

$$HV10 = 0.47\,P/a^2 \quad (1)$$

where $HV10$ is the Vickers hardness, P is the load applied and a is half the length of the diagonal of the indentation produced by the indenter. The fracture toughness (K_{1C}) has been evaluated using the indentation fracture (IF) toughness technique. In this study, the indentation fracture toughness K_{1C} (MPa $m^{1/2}$) was calculated using the appropriate formula proposed by Niihara et al. [33] for median cracks

$$K_{1C} = 0.018 \times HV \times a^{0.5}(E/HV)^{0.4}(c/a-1)^{-0.5} \times (\text{for } c/a < 3.5 \text{ and } l/a < 2.5) \quad (2)$$

where $2a$ is the average indent diagonal length (μm), $2c$ is the crack length (from one crack tip to another), E is the elastic modulus (GPa) which is taken as a constant equivalent to 320 GPa for all the samples and H is the measured hardness (GPa). Both the indent diagonal and crack length were carefully measured from optical images of the indented surfaces and the reported hardness and fracture toughness values were the average of at least five indentation measurements. The indentation damage behavior of materials was studied in detail using SEM. The microstructural investigation of the polished surfaces of samples was performed by means of a scanning electron microscope (SEM-ZEISS Supra 40VP) in the back-scattered electron imaging mode.

The types of crystalline phases and the α^{1}:β^{1}-SiAlON phase ratios were determined by means of X-ray diffraction analyses (XRD-Panalytical, Empyrean with Cu-Kα radiation). The α^{1}:β^{1}-SiAlON phase ratios were found by quantitative estimation

from the XRD patterns using the integrated intensities of the (102) and (210) reflections of α'-SiAlON and the (101) and (210) reflections of β'-SiAlON by the following equation:

$$\frac{I_\beta}{I_\beta + I_\alpha} = \frac{1}{1 + K\left[(1/w_\beta) - 1\right]} \quad (3)$$

where I_α and I_β are the observed intensities of α'- and β'-SiAlON peaks, respectively, w_β is the relative weight fraction of β-SiAlON, and K is the combined proportionality constant resulting from the constants in the two equations, namely:

$$I_\beta = K_{\beta^*} W_\beta \quad (4)$$

$$I_\alpha = K_{\alpha^*} W_\alpha \quad (5)$$

which is 0.518 for β (101) − α (102) reflections and 0.544 for β (210) − α (210) reflections [34]. Since thermal shock test results indicate the sample surface characteristics, α':β'-SiAlON phase ratios were measured on the sample surfaces.

The z-value of the β-SiAlON phase was obtained from the mean of the z_a and z_c values given by the following equations:

$$z_a = \frac{a - 7.6044}{0.031} \quad (6)$$

$$z_c = \frac{c - 2.9075}{0.026} \quad (7)$$

where a and c are the calculated unit cell dimensions of β-SiAlON: JCPDS card 33-1160 was used as a reference for β-Si_3N_4 where $a = 7.6044(2)$ Å and $c = 2.9075(1)$ Å.

For the thermal diffusivity measurements, disks of 13 mm diameter were ground to 2 mm thickness. Both sides of the samples were coated with gold and carbon. Gold prevents the direct transmission of the beam and improves energy transfer to the sample, while carbon increases the absorption of the front surface and the emission of the back surface. The measurements were performed between RT and 1073 K using the laser-flash method (Netzsch LFA 457, Selb, Germany). Each data point represented the mean of four individual measurements, with a variation of ±0.1%. Measurements were carried out under a flowing nitrogen gas atmosphere at a flow rate of 100 mbar/s.

Thermal diffusivity (a) was determined by the following formula:

$$\alpha = W_x d^2 / \pi^2 t_x \quad (8)$$

where W_x is a dynamic correction factor to account for the heat losses, d is the thickness of the specimen, and t_x is the time for the test piece for the initiation of the pulse. After the density (ρ) measurement by the Archimedes method and specific heat (Cp) measurement by a differential scanning calorimeter, the thermal conductivity (k) of samples weres calculated according to the equation [35]:

$$k = \rho \mathrm{Cp} \alpha \quad (9)$$

2.3. Thermal shock measurements

The thermal shock resistance was measured by the indentation-quench method developed by Anderson and Rowcliffe [28]. Cylindrical samples, with a diameter of 12 mm were used in all test series. The samples were ground to obtain mutually parallel two surfaces, and one side was then polished down to 1 μm diamond suspension. Well-defined cracks were initiated with a Vickers indenter (Emco Test, Duroscan20, Struers, Avustria). Four indents were made on each sample, and each indent generated four cracks, so that 16 cracks were made on each sample. The following parameters were held constant: the sample thickness was 4.0 ± 0.5 mm, the initial crack length was 107 ± 0.2 μm and the water bath temperature was 90 °C. Pettersonn et al. [29] reported that the water bath temperature was found to be critical for the crack growth induced by quenching. They have advised 90 °C bath temperature for the best thermal shock resistance measurements. A thermostat was used to control the water-bath temperatures. The crack length was measured with an optical microscope which was attached to Vickers indenter. The samples were heated in an air atmosphere upto 490, 690 and 890 °C in a muffle furnace, with a holding time of 20 min, and subsequently quenched in the water bath.

The furnace temperature was selected to give the desired temperature difference, ΔT. The crack growth was measured for each temperature difference, and the crack growth (ΔC) was calculated as the percentage of the initial crack length. The thermal shock properties were evaluated at various ΔT-values for SiAlON and SiAlON–TiN composites. When the test specimens were heated in air, and a slight oxidation was observed at the highest temperature.

3. Results and discussion

3.1. The materials

The samples S0, S10T, S17T and S25T, contain 0%, 10%, 17% and 25% TiN in SiAlON matrix, respectively. Both ceramic samples were fully densified, and the measured densities are listed in Table 1. The density was confirmed by

Table 1
Phase evolution, z values and mechanical properties of sintered SiAlON and SiAlON–TiN samples.

Sample	β':α' ratio (%) (powdered)	β':α' ratio (%) (from surface)	Measured z value	Type of IGP	Bulk density (g/cm^3)	Open porosity (%)	$HV10$ (GPa) (from surface)	K_{ic} (MPa m$^{1/2}$) (from surface)
S0	79β':21α'	61β':39α'	0.65	S'	3.3586	0.03	16.60 ± 0.3	6.4 ± 0.4
S10T	78β':22α'	80β':20α'	0.66	S', M'	3.4860	0.04	16.00 ± 0.1	7.5 ± 0.1
S17T	76β':24α'	83β':17α'	0.66	M'	3.5793	0.01	16.10 ± 0.1	8.0 ± 0.1
S25T	77β':23α'	88β':12α'	0.66	M'	3.6858	0.03	15.60 ± 0.2	8.2 ± 0.2

S': $Er_2Si_2O_7$ and M': $ErSi_2Al_2O_{6.8}N_{1.13}$.

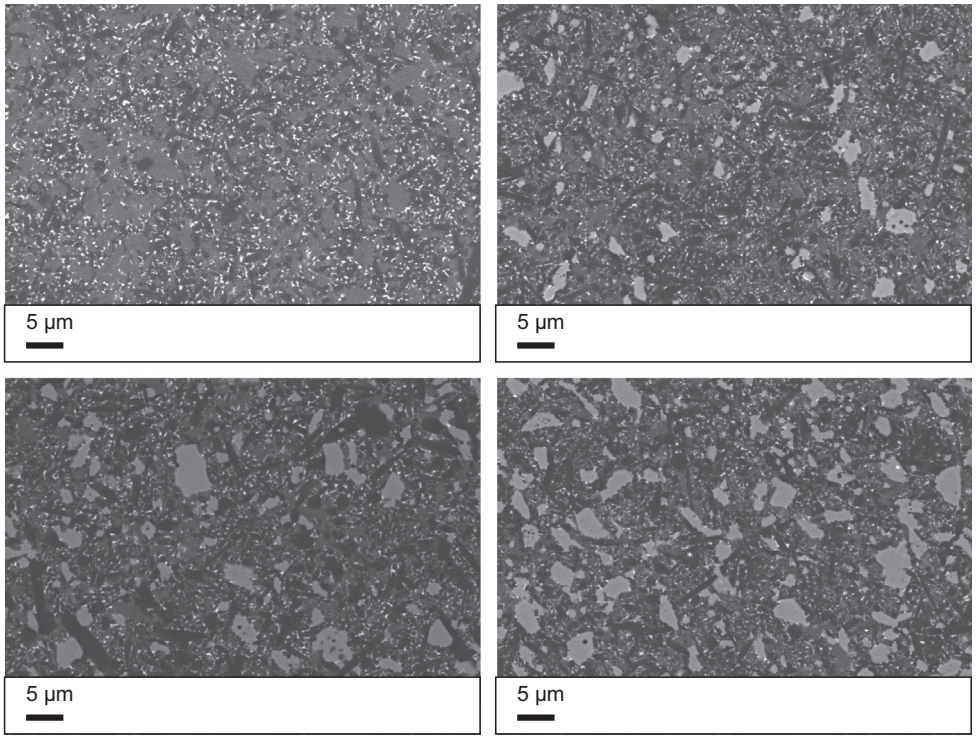

Fig. 1. SEM micrographs of polished surfaces of (a) S0, (b) S10T, (c) S17T and (d) S25T recorded in BSE mode.

SEM images of the polished surfaces, i.e. no pores or voids were observed. Micrographs of polished surfaces of samples are shown in Fig. 1. TiN particles were found to be homogeneously dispersed in the SiAlON matrix. Addition of TiN particles caused β-SiAlON grain structure to become elongated due to the increase in intergranular phase content accompanied by the presence of a TiO_2 layer on TiN particles. Therefore S25T had the highest fracture toughness, but the hardness of the sample was less since it had lower α-SiAlON phase content (Table 1).

The melilite ($LnSi_2Al_2O_{6.8}N_{1.13}$) and silicate phases ($Ln_2Si_2O_7$) were observed other than α-SiAlON, β-SiAlON and TiN crystalline phases in all SiAlON and SiAlON–TiN composites (Fig. 2). It is obvious that the crystallization tendency of intergranular phase changed with the addition of TiN reinforcement phase. Disilicate phase ($Er_2Si_2O_7$) was observed for S0 sample, whilst melilite phase was formed by the incorporation of TiN phase. S17 and S25 samples had single melilite phase crystallization; on the other hand S10 sample had melilite and silicate phase crystallization together. This phenomenon can be explained by the change in intergranular phase chemistry due to TiN addition. SiO_2 in the liquid phase decreases with an increase of TiN in the composite. This can explain the decrease in silicate phase with the increase in TiN content. TiN provided more nitrogen in liquid phase, so melilite phase (rich in nitrogen content) crystallization was obtained. 10 wt % TiN addition provided both melilite and silicate phase stabilization. The melilite phase is well known as a good secondary refractory phase which displays good high temperature stability since it has very high nitrogen content [17]. On the other hand, $Er_2Si_2O_7$ phase is oxidation resistant and it has a number of advantages for high temperature applications. In addition, similar α':β' phase ratios were achieved for all of the

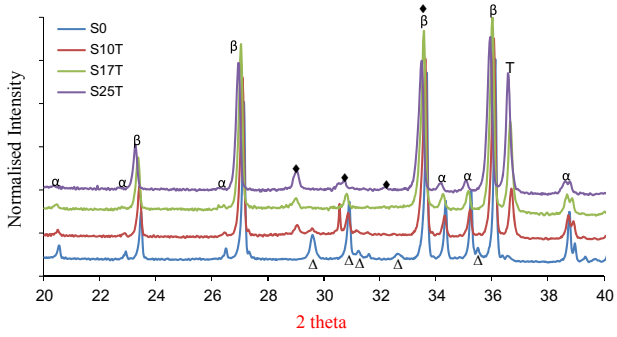

Fig. 2. XRD pattern of SiAlON and SiAlON–TiN compositions which have different amount of TiN particles.

compositions obtained from powdered form (see Table 1). Small differences in the surface α':β' phase ratios were observed due to polishing depth of samples. α' phase amount was higher due to the faster cooling. In the SO sample α' phase was higher in the regions closer to the surface.

The z value of β' phase did not change with TiN addition (see Table 1) and remained ~0.7 in the samples. The similar phenomenon was observed by Johnson et al., [36] and Acikbas [37]. The morphology of β' grains varied with the amount of TiN particles added, as seen in Fig. 1. More elongated grains were achieved for 25 wt% TiN added sample. It was mainly due to the presence of a TiO_2 layer on TiN particles. Further addition of TiN brought about more TiO_2 layer and increased the liquid phase during sintering. TiN might have lowered the liquid phase viscosity and has been instrumental in the crystallization of more melilite phase.

The effect of the TiN and its amount on the Vickers hardness and indentation fracture toughness is shown in Fig. 3. The hardness decreased with TiN addition and increased with TiN content, as the fraction of hard α-SiAlON phase decreased with TiN addition and soft intergranular phase content increased. Therefore S0 sample had the highest hardness due to highest amount of α-SiAlON phase and least intergranular phase content. The fracture toughness improved with increasing TiN content and the highest value, 8.2 ± 0.2 MPa $m^{1/2}$, was reached for the S25T sample with 25 wt% TiN content due to presence of high aspect ratio grains (see Fig. 1). Moreover, the presence of TiN particles, which had a higher coefficient of thermal expansion compared to SiAlON phases, led to compressive stresses in the matrix which was instrumental in a crack deflection mechanism and resulted in a higher fracture toughness. All samples showed intergranular fracture mode in the matrix and it was deduced that the improvement in toughness with increasing intergranular phase content was due to deflection of cracks encountering bimodal grain structures, as shown in Fig. 4. For all three different TiN contents the fracture toughness was improved by the addition of 25 wt% TiN particles.

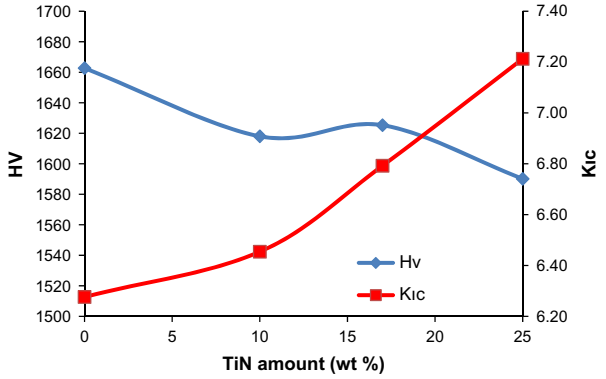

Fig. 3. Fracture toughness and hardness versus TiN content.

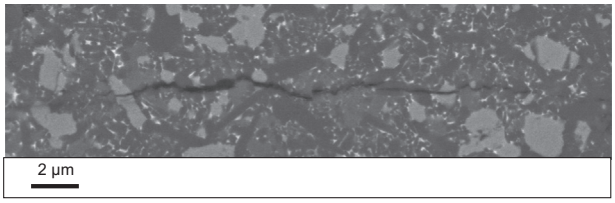

Fig. 4. Crack profile of S25T sample.

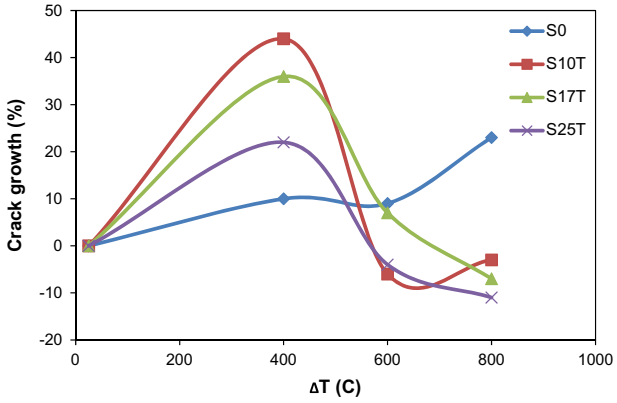

Fig. 5. Thermal shock resistance measuremt showing crack growth versus temperature difference curves for all samples.

3.2. Thermal shock resistance

The crack growth (ΔC) versus the thermal shock temperature difference (ΔT) is shown in Fig. 5. for SiAlON and SiAlON–TiN composites. Stable crack extension was observed

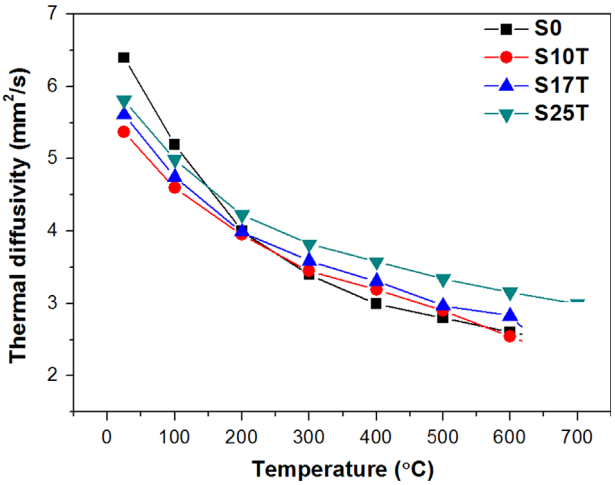

Fig. 6. Thermal diffusivity versus temperature diagram for SiAlON and SiAlON–TiN composites.

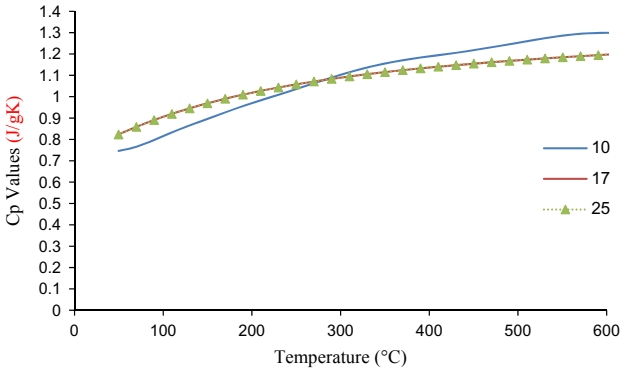

Fig. 7. Cp values versus temperature diagram for different SiAlON–TiN composites.

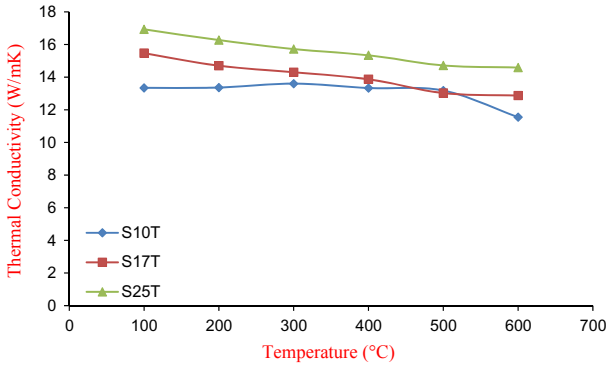

Fig. 8. Thermal conductivity values versus temperature diagram for different SiAlON–TiN composites.

within the whole temperature intervals for all of the samples. It is evident that the thermal shock resistance of SiAlON was improved by the addition of TiN phase. As can be seen in Fig. 5. crack growth rate was changing with the existence of TiN and its amount. The best thermal shock resistance was achieved at a high fraction of TiN. Increasing the fraction of TiN phase increased the thermal shock resistance, and the α:β-SiAlON without TiN had the poorest thermal shock behavior among all the samples. Besides, α:β SiAlON phase ratio affected the thermal shock resistance. S0 sample had the highest α phase content (39 wt% α phase) corresponding to the poorest thermal shock behavior. The morphology of the grains in the composite also might have an influence on the thermal shock properties. The α phase was equiaxed and β-phase was elongated. For instance, S25T sample (88 wt% β phase) showed better thermal shock behavior for which most of the β-SiAlON grains were elongated. Elongated grains improved the thermal shock resistance by providing energy consuming mechanisms such as crack deflection and/or bridging hindering the crack extension. The presence of TiN in high amounts provided more liquid phase formation during sintering. In turn, the presence of more liquid phase during sintering enhanced the grain growth, so that more elongated grains with high aspect ratio were formed (Fig. 1). So one of the reasons that S25T sample had the highest thermal shock resistance was the elongated grain morphology.

Another important factor that influences the thermal shock resistance of a material is the thermal conductivity. It is generally accepted that higher the grain size, the higher is the thermal conductivity [38]. In the present study, it was observed that the grain growth became more prominent as the TiN content increased. At ambient temperature S0 sample had slightly higher thermal diffusivity values than the other samples (Fig. 6). When the temperature increased to 200 °C, S25T sample had higher thermal diffusivity values. However, TiN addition had no observable effect on thermal diffusivity (Fig. 6). Fig. 7 shows the measured heat capacity values of the samples. The temperature dependence of the heat capacities of

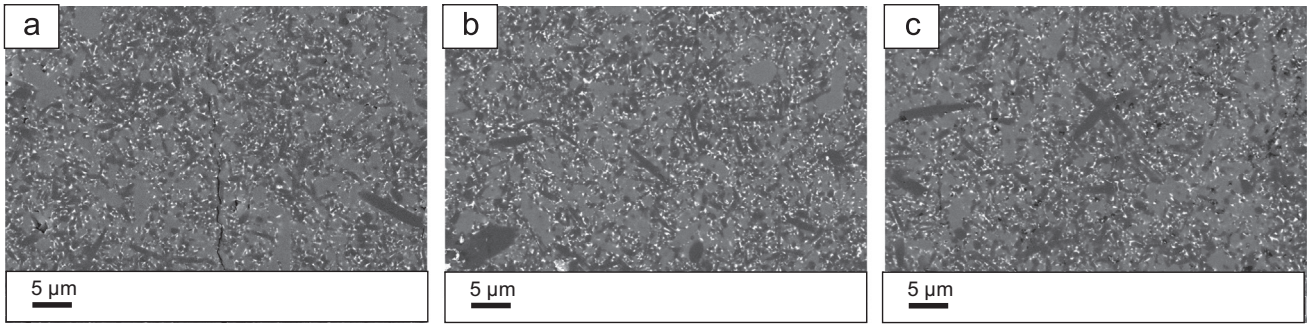

Fig. 9. SEM images of S0 samples after thermal shock tests at different temperature differences (Δ*T*) (a) 400 °C, (b) 600 °C, and (c) 800 °C.

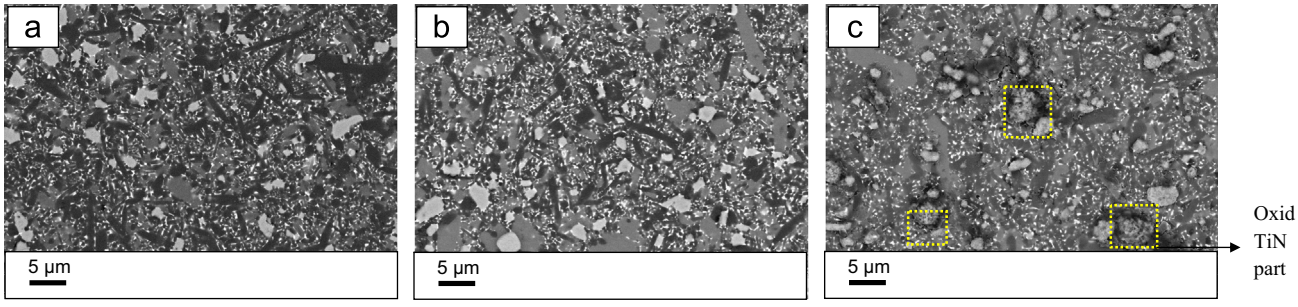

Fig. 10. SEM images of S10T samples after thermal shock tests at different temperature differences (Δ*T*) (a) 400 °C, (b) 600 °C, and (c) 800 °C.

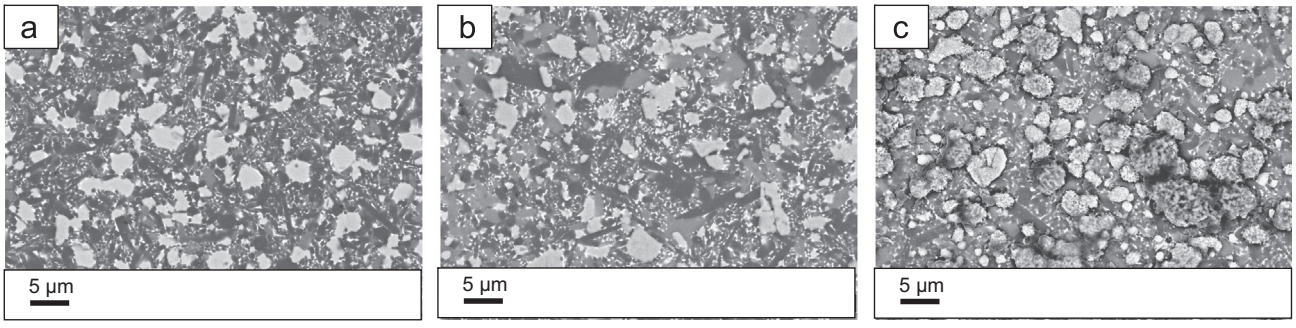

Fig. 11. SEM images of S17T samples after thermal shock tests at different temperature differences (Δ*T*) (a) 400 °C, (b) 600 °C, and (c) 800 °C.

the samples S17T and S25T was exactly the same. The sample S10T showed a different trend that while the heat capacity was relatively low at lower temperatures, it increased at higher temperatures (500–600 °C). The thermal conductivity values of the samples were calculated by Eq. (9), and the results are shown in Fig. 8. The thermal conductivity of the sample S25T was the highest independent of temperature. The thermal conductivity increased with the increasing TiN amount for all of the samples. Since high thermal conductivity is a factor suppressing crack propagation, the samples with higher thermal conductivities had a lower tendency for crack propagation (Fig. 5).

At the first glance it proved hard to assess the influence of intergranular phase chemistry on the thermal shock behavior of the samples. K_{ic} increased with the increasing TiN amount; nevertheless, silicate was changing to melilite simultaneously affecting the intergranular phase chemistry.

In order to further evaluate the thermal shock resistance behavior, SEM images of the samples were taken after the thermal shock tests at various temperatures (Figs. 9–12). S0 sample without TiN showed more oxidation resistance than others. The oxidation of titanium nitride to rutile (TiO_2) started at a temperature lower than for Si_3N_4, between 500 and 600 °C [39]. It was observed that the oxidation was controlled via oxygen diffusion through TiO_2 layer, especially, at temperatures below 1000 °C [40–43]. Under oxidation conditions the TiN particles were partially oxidized to a TiO_2 phase (Figs. 10c, 11c, and 12c). TiO_2 filled the cracks and provided crack healing. Therefore, sample S25T showed the best thermal shock resistance behavior. TiO_2 phase evolution after thermal shock tests were detected by XRD and SEM–EDX analyses for TiN added samples (see Fig. 13, and Table 2).

Up to 400 °C, crack propagation was insignificant for the S0 sample. The crack growth rate was nearly constant between 400 and 600 °C. Above 600 °C, crack growth rate increased. TiN added samples showed higher crack growth rates than the S0 sample. S10T sample had the highest crack growth rate between 25 and 400 °C. Above 400 °C, TiN oxidation started providing crack healing, and hence crack growth rate lowered. S17T and S25T samples showed similar tendencies for crack propagation. On the other hand S10T sample showed an increased crack growth rate above 600 °C. When the TiN amount was larger than 10%, significant crack healing behavior was observed.

4. Conclusions

SiAlON and SiAlON–TiN composites containing various amounts of TiN were produced in order to evaluate the effect of TiN particles on the thermal shock properties. The indentation-quench experiments were used to determine the thermal behavior of the sintered materials. The microstructure of SiAlON–TiN composites consisted of elongated grains, and the addition of TiN positively affected the elongated grain morphology of β-SiAlON grains. The fracture toughness increased with the increasing TiN amount. The maximum values of the fracture toughness were obtained in SiAlON–TiN composites containing 25 wt% TiN particles. The addition of TiN particles had little effect on the hardness values of SiAlON–TiN composites. SiAlON–TiN composites exhibited a superior thermal shock property when the amount of TiN was 25 wt%. The addition of TiN also improved the resistance to thermal shock damage, and SiAlON–TiN composites with 25 wt% TiN particles having the best capability

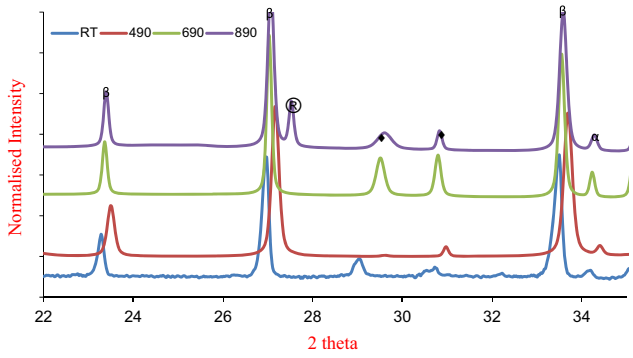

Fig. 13. XRD pattern of S25T samples before and after thermal shock tests at different temperature intervals (®: TiO_2 (Rutile)).

Table 2
EDX analysis result of S17T sample after thermal shock test at 890 °C (Pt belongs to conductive coating).

Element	wt%
Oxygen	38.9
Silicon	1.1
Erbium	0.4
Titanium	55.7
Aluminum	0.4
Platinum	3.5

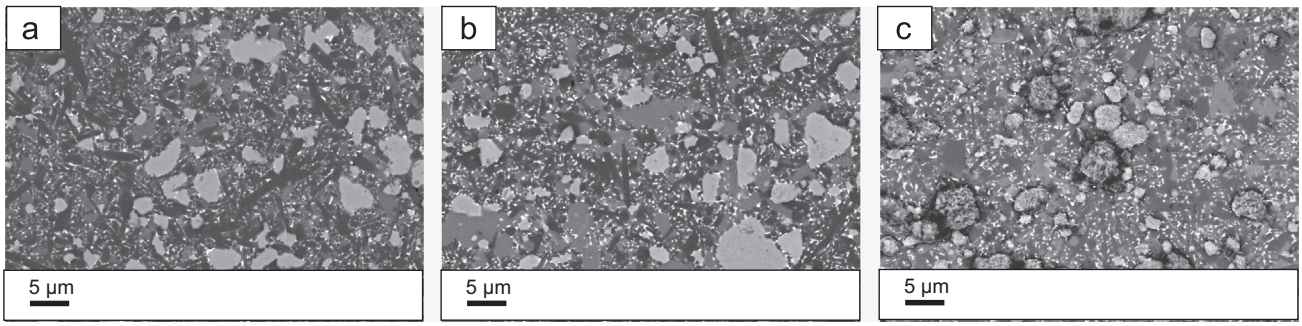

Fig. 12. SEM images of S25T samples after thermal shock tests at different temperature differences (ΔT) (a) 400 °C, (b) 600 °C, and (c) 800 °C.

to suppress crack propagation achieved by passive oxidation above 700 °C.

Acknowledgment

The authors gratefully acknowledge the financial support provided by Bilecik Seyh Edebali University (Project no.: 2011-01-BİL.01-002) instrumental in the completion of the study reported in this manuscript.

References

[1] T. Ekström, M. Nygren, SiAlON ceramics, Journal of the American Ceramic Society 75 (1992) 259–276.
[2] G.C. Deeley, J.M. Herbert, N.C. Moore, Dense silicon nitride, Powder Metallurgy 8 (1961) 145–151.
[3] M. Mitomo, Y. Tayima, Sintering, properties and applications of silicon nitride and SiAlON ceramics, Journal of the Japanese Ceramic Society 99 (1991) 1014.
[4] G.R. Terwilliger, Properties of sintered Si_3N_4, Journal of the American Ceramic Society 57 (1974) 48–49.
[5] Ceramic Matrix Composites: Microstructure/Property Relationship, Woodhead Publishing Ltd., ISBN-10/ASIN: 1855739429, 2006.
[6] Y.G. Gogotsi, Review-particulate silicon nitride-based composites, Journal of Materials Science 29 (1994) 2541–2556.
[7] P. Pettersson, M. Johnsson, Thermal shock properties of alumina reinforced with Ti(C, N) whiskers, Journal of the European Ceramic Society 23 (2003) 309–313.
[8] M.E. Ebrabimi, J. Chevalier, G. Fantozzi, Slow crack growth behavior of alumina ceramics, Journal of Materials Research 15 (1) (2000) 142–147.
[9] H.J. Cho, K.S. Cho, J.G. Lee, R-curve behavior of silicon nitride-titanium nitride composites, Journal of the American Ceramic Society 80 (10) (1997) 2681–2684.
[10] E. Ayas, A. Kara, H. Mandal, S. Turan, F. Kara, Production of α-β SiAlON–TiN/TiCN composites by gas pressure sintering, Silicates Industriels 69 (2004) 287–292.
[11] S. Boskovic, F. Sigulinski, L. Zivkovic, Liquid-phase sintering and properties of Si_3N_4–TiN composites, Journal of Materials Synthesis and Processing 7 (2) (1999) 119–126.
[12] R.G. Duan, G. Roebben, J. Vleugels, O. Biest, Optimization of microstructure and properties of in situ formed β-O-SiAlON–TiN composite, Materials Science and Engineering: A 427 (2006) 195–202.
[13] T. Ekström, P.O. Olsson, β-SiAlON ceramics with TiN particle inclusions, Journal of the European Ceramic Society 13 (6) (1994) 551–559.
[14] L. Gao, J. Li, T. Kusunose, K. Niihara, Preparation and properties of TiN–Si_3N_4 composites, Journal of the European Ceramic Society 24 (2004) 381–386.
[15] T. Hirai, S. Hayashi, Preparation and Some properties of chemically vapour-deposited Si_3N_4–TiN composite, Journal of Materials Science 17 (1982) 1320–1328.
[16] B. Lee, S. Hayashi, T. Hirai, K. Hiraga, Crack propagation behavior of CVD Si_3N_4–TiN composite examined by high-resolution electron microscopy, Materials Transactions: Japan Institute of Metals 34 (1993) 573–579.
[17] T. Nagaoka, M. Yasuoka, K. Hira, S. Kanzaki, Effects of TiN particle-size on mechanical-properties of Si_3N_4/TiN particulate composites, Journal of the Ceramic Society of Japan 100 (1992) 617–620.
[18] A. Bellosi, S. Guicciardi, A. Tampieri, Development and characterization of electroconductive Si_3N_4–TiN composites, Journal of the European Ceramic Society 9 (1992) 83–93.
[19] F. Hong, R.J. Lumby, M.H. Lewis, TiN/SiAlON composites via in-situ reaction sintering, Journal of the European Ceramic Society 11 (1993) 237–239.
[20] T. Jiang, X. Xue, Z. Li, P. Duan, High temperature oxidation behavior of electroconductive TiN/O′–SiAlON ceramics prepared from high titania slag-based mixture, Transactions of Nonferrous Metals Society of China 21 (2011) 2638–2643.
[21] B. Lee, Y.J. Yoon, K.H. Lee, Microstructural characterization of electro-conductive Si_3N_4–TiN composites, Materials Letters 47 (2001) 71–76.
[22] C.C. Liu, J.L. Huang, Micro-electrode discharge machining of TiN/Si_3N_4 composites, British Ceramic Transactions 99 (4) (2000) 149–152.
[23] C. Titan, H. Jiang, N. Liu, Thermal shock behavior of Si_3N_4–TiN nano-composites, International Journal of Refractory Metals and Hard Materials 29 (2011) 14–20.
[24] S.S. Manson, R.W. Smith, Theory of thermal shock resistance of brittle materials based on Weibull's statistical theory, Journal of the American Ceramic Society 38 (1) (1955) 18–27.
[25] D.H. Hasselman, Fracture ınitiation and crack propagation in brittle ceramics, Journal of the American Ceramic Society 52 (11) (1969) 600–604.
[26] D.P.H. Hasselman, Strength behavior of polycrystalline. alumina subjected to thermal shock, Journal of the American Ceramic Society 53 (1970) 490–494.
[27] P.F. Becher, D. Lewis III, K.R. Carman, A.C. Gonzalez, Thermal shock resistance of ceramics size and geometry effects in quench tests, American Ceramic Society Bulletin 59 (1980) 542–545.
[28] T. Andersson, D.J. Rowcliffe, Indentation thermal shock test for ceramics, Journal of the American Ceramic Society 79 (1996) 1509–1514.
[29] P. Pettersson, M. Johnsson, Z. Shen, Parameters for measuring the thermal shock of ceramic materials with an indentation-quench method, Journal of the European Ceramic Society 22 (2002) 1883–1889.
[30] P. Pettersson, Z. Shen, M. Johnsson, M. Nygren, Thermal shock resistance of α:β-SiAlON ceramic composites, Journal of the European Ceramic Society 21 (2001) 999–1005.
[31] P. Pettersson, Z. Shen, M. Johnsson, M. Nygren, Thermal shock properties of β-SiAlON ceramics, Journal of the European Ceramic Society 22 (2002) 1357–1365.
[32] A.G. Evans, E.A. Charles, Fracture toughness determinations by indentation, Journal of the American Ceramic Society 59 (1976) 371–372.
[33] K. Niihara, R. Morena, P.H. Hasselman, Evaluation of K_{1c} of brittle solids by the indentation method with low crack-to-indent ratios, Journal of Materials Science Letters 1 (1982) 13–16.
[34] K. Liddell, X-ray analysis of nitrogen ceramic phases (M.Sc. thesis), University of Newcastle upon Tyne, UK, 1979.
[35] S.R. Kushan, I. Uzun, B. Dogan, H. Mandal, Experimental and finite element study of the thermal conductivity of a-SiAlON ceramics, Journal of the American Ceramic Society 90 (12) (2007) 3902–3907.
[36] Z. Zhao, M. Johnsson, Z.J. Shen, Microstructure and mechanical properties of titanium carbonitride whisker reinforced β-SiAlON matrix composites, Materials Research Bulletin 37 (2002) 1175–1187.
[37] N. Calis Acikbas, O. Demir, The effect of cation type, intergranular phase amount and cation mole ratios on z value and intergranular phase crystallisation of SiAlON ceramics, Ceramics International 39 (3) (2013) 3249–3259.
[38] W.D. Kingery, Factors affecting thermal stress resistance of ceramic materials, Journal of the American Ceramic Society 38 (1) (1955) 3–15.
[39] Y. Yin, L. Hang, S. Zhang, X.L. Bui, Thermal oxidation properties of titanium nitride and titanium–aluminum nitride materials—A perspective for high temperature air-stable solar selectiveabsorber applications 515 (2007) 2829–2835Thin Solid Films 515 (2007) 2829–2835.
[40] A. Bellosi, A. Tamperieri, Y.Z. Liu, Oxidation behaviour of electro-conductive Si_3N_4–TiN composites, Materials Science and Engineering A 127 (1990) 115–122.
[41] J. Desmaison, P. Lefort, M. Billy, Oxidation mechanism of TiN in oxygen, Oxidation of Metals 13 (6) (1979) 505–517.
[42] H. Ichimura, A. Kawana, High temperature oxidation of ion-implanted TiN and TiAlN films, Journal of Materials Research 8 (5) (1993) 1093–1100.
[43] F. Deschaux-Beaume, N. Frety, T. Cutard, C. Colin, Oxidation modeling of a Si_3N_4–TiN composite: comparison between experiment and kinetic models, Ceramics International 35 (2009) 1709–1718.